Electronic Supplementary Material (ESI) for Journal of Materials Chemistry C.

Cunning defects: Emission control by structural point defects on Cu(I)I double chain Coordination Polymers

Javier Conesa-Egea,[a,b] Javier González-Platas,[c] Ulises R. Rodríguez-Mendoza,[c] José Ignacio Martínez,[d] Pilar Ocon,[e] Vanesa Fernández-Moreira,[f] Rubén D. Costa,[g] Julio Fernandez-Cestay,[g] Félix Zamora,[a,b,h] and Pilar Amo-Ochoa[a,h]*

Supporting Information

S1. Structural characterization of 1 and 1’.

S1.1. Single crystal X-ray diffraction (SCXRD) analysis of 1 and 1’.

The structure of **[Cu(Cl$_2$-py)I]$_n$**, shaped as both **1** and **1’**, is defined by a very simple asymmetric unit (Figure S1). When this asymmetric unit is extended, a polymeric motif defined by a double Cu-I *zigzag* chain is created (Figure S2).

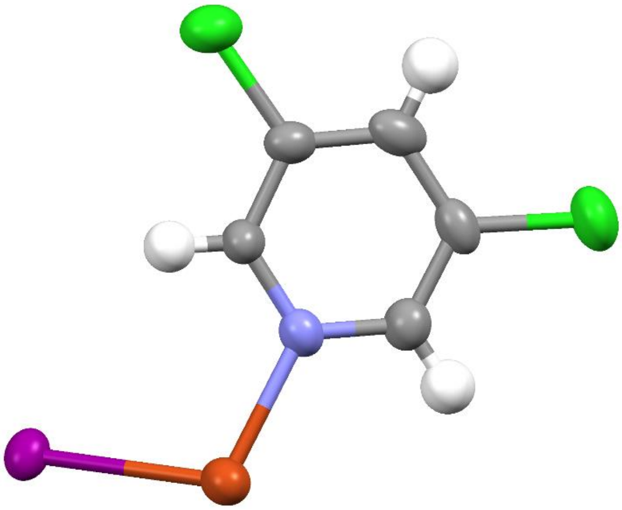

Figure S1. Thermal ellipsoid plot (50%) of the asymmetric unit of **[Cu(Cl$_2$-py)I]$_n$** at room temperature and pressure. Grey: C; white: H; blue: N; green: Cl; orange: Cu; purple: I.

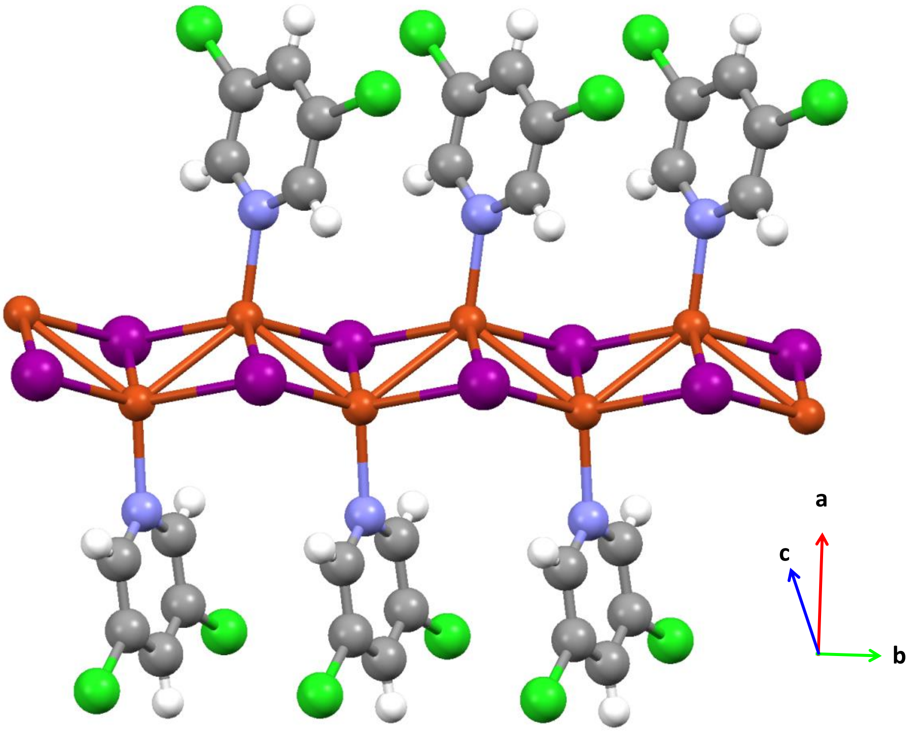

Figure S2. View of the double-stranded staircase motif of **[Cu(Cl$_2$-py)I]$_n$**. The chain grows parallel to the *b* axis.

Table S1. Crystal structure parameters of **1** and **1'**.

	1 (296 K)	**1 (110 K)**	**1' (296 K)**
Empirical formula	$C_5H_3Cl_2CuIN$	$C_5H_3Cl_2CuIN$	$C_5H_3Cl_2CuIN$
Formula weight	338.42	338.42	338.42
Space group	$P2_1/c$	$P2_1/c$	$P2_1/c$
Crystal System	Monoclinic	Monoclinic	Monoclinic
a (Å)	13.1164(6)	12.961(2)	13.1301(6)
b (Å)	4.2363(2)	4.2177(5)	4.2377(2)
c (Å)	15.1474(5)	15.008(2)	15.1614(7)
α (°)	90	90	90
β (°)	94.613(4)	94.247(5)	94.623(4)
γ (°)	90	90	90
V (Å^3)	838.94(6)	818.2(2)	840.86(7)
Z	4	4	4
ρ_{calc} (g·cm^{-3})	2.679	2.747	2.673
***F*(000)**	624	624	624
μ (mm^{-1})	6.840	7.013	6.824
Reflections collected/R_{int}	3723/0.0189	12661/0.0320	2141/0.0160
Unique data/restraints/parameters	2059/0/91	1495/0/91	1211/0/91
Goodness of fit (*S*)	1.089	1.280	1.079
***R*1/*wR*2 [$I>2\sigma(I)$]**	0.0330/0.0550	0.0144/0.0420	0.0223/0.0425
***R*1/*wR*2 [all data]**	0.0464/0.0596	0.0200/0.0699	0.0291/0.0454

Table S2. Selected distances (Å) and angles (°) of **1** and **1'**.

	1 (296 K)	**1 (110 K)**	**1' (296 K)**
Cu-I1$_{rail}$	2.6159(6)	2.6163(6)	2.6173(6)
Cu-I1$^{i}_{rail}$	2.6812(6)	2.6742(6)	2.6832(6)
Δ[Cu-I1$_{rail}$]	0.0653	0.0579	0.0659
Cu-I1$_{rung}$	2.6415(6)	2.6352(6)	2.6427(7)
Cu-N1	2.083(3)	2.084(3)	2.083(4)
Cu-Cu^{ii}	2.8092(7)	2.7689(6)	2.8118(8)
Cu-Cu^{iii}	2.8092(7)	2.7689(6)	2.8118(8)
Δ[Cu-Cu]	0.000	0.000	0.000
I1-Cu1-I1^{i}	106.20(2)	105.73(2)	106.16(2)
I1-Cu1-I1^{ii}	116.97(2), 114.72(2)	117.77(2), 115.72(2)	116.95(2), 114.68(2)
I1^{i}-Cu1-I1^{i}	114.72(2), 116.97(2)	115.72(2), 117.77(2)	114.68(2), 116.95(2)
Cu1-I1-Cu1^{ii}	64.59(2), 63.70(2)	63.64(1), 62.86(1)	64.63(2), 63.73(2)
Cu1-I1-Cu1^{iii}	106.20(2)	105.73(2)	106.16(2)
Cu1^{ii}-I1-Cu1^{iii}	63.70(2), 64.59(2)	62.86(1), 63.64(1)	63.73(2), 64.63(2)
I1-Cu1-N1	110.3(1)	109.65(9)	110.3(1)
I1^{i}-Cu1-N1	101.8(1)	105.1(1)	101.9(1)
Dihedral angle	125.38	127.22	125.25
Tilt angle	89.89	89.62	89.86
Twist angle	59.15	58.43	59.17
Interchain distance	2.834	2.730	2.839

Symmetry codes: i) x-1, y, z; ii) -x, -y, -z+1; iii) -x+1, -y, -z+1

S1.2. Powder X-ray diffraction (PXRD) characterization of 1 and 1'.

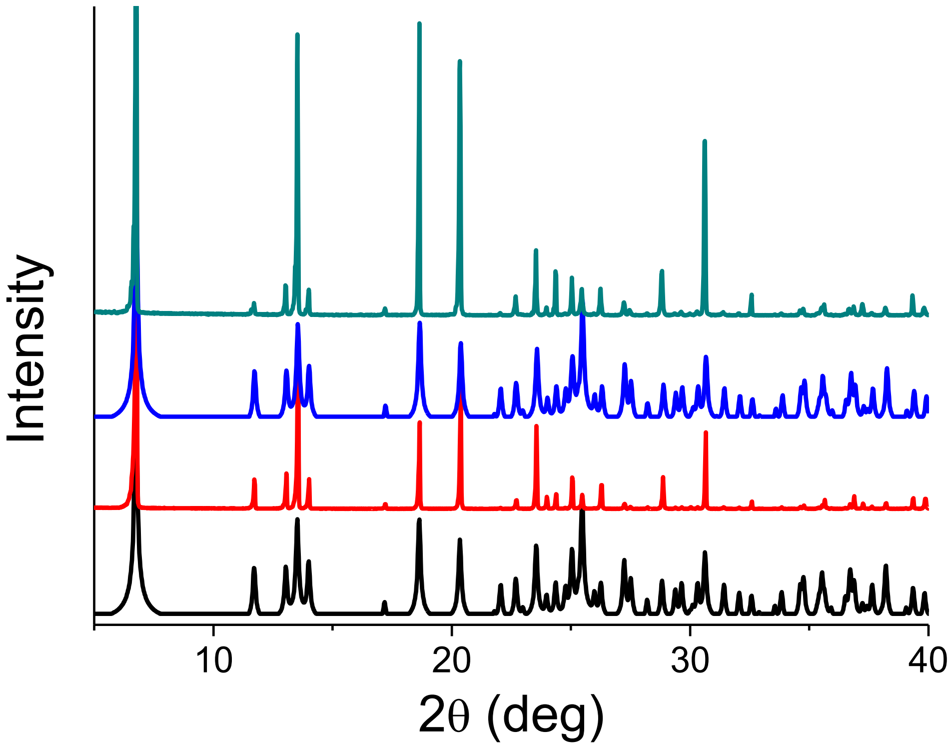

Figure S3. Powder X-ray diffraction patterns of **1** (simulated in black, experimental in red) and **1'** (simulated in blue, experimental in green).

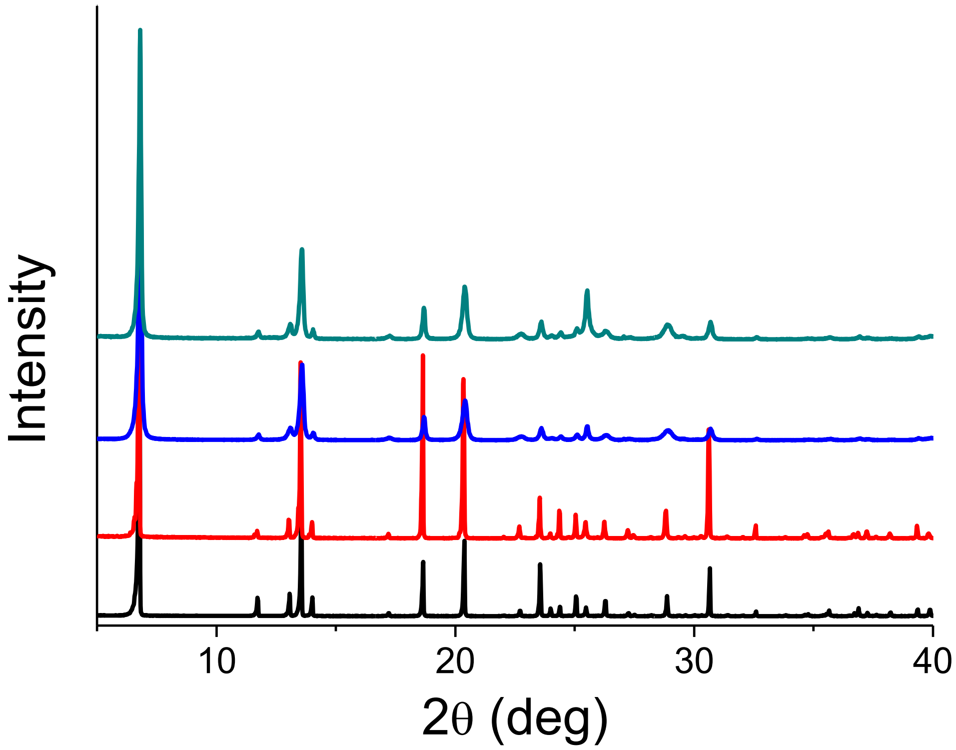

Figure S4. Powder X-ray diffraction patterns of **1** and **1':** pristine solid (**1** in black, **1'** in red) and pellets pressed at 5 GPa (**1** in blue, **1'** in green).

S1.3. High pressure X-ray diffraction analysis.

The differences between samples were negligible as can be observed on Figure S6 except for *b*-axis. However, compound **1** deteriorated after exceeding pressures of 6 GPa, so for the rest of experiments we will focus on compound **1’**.

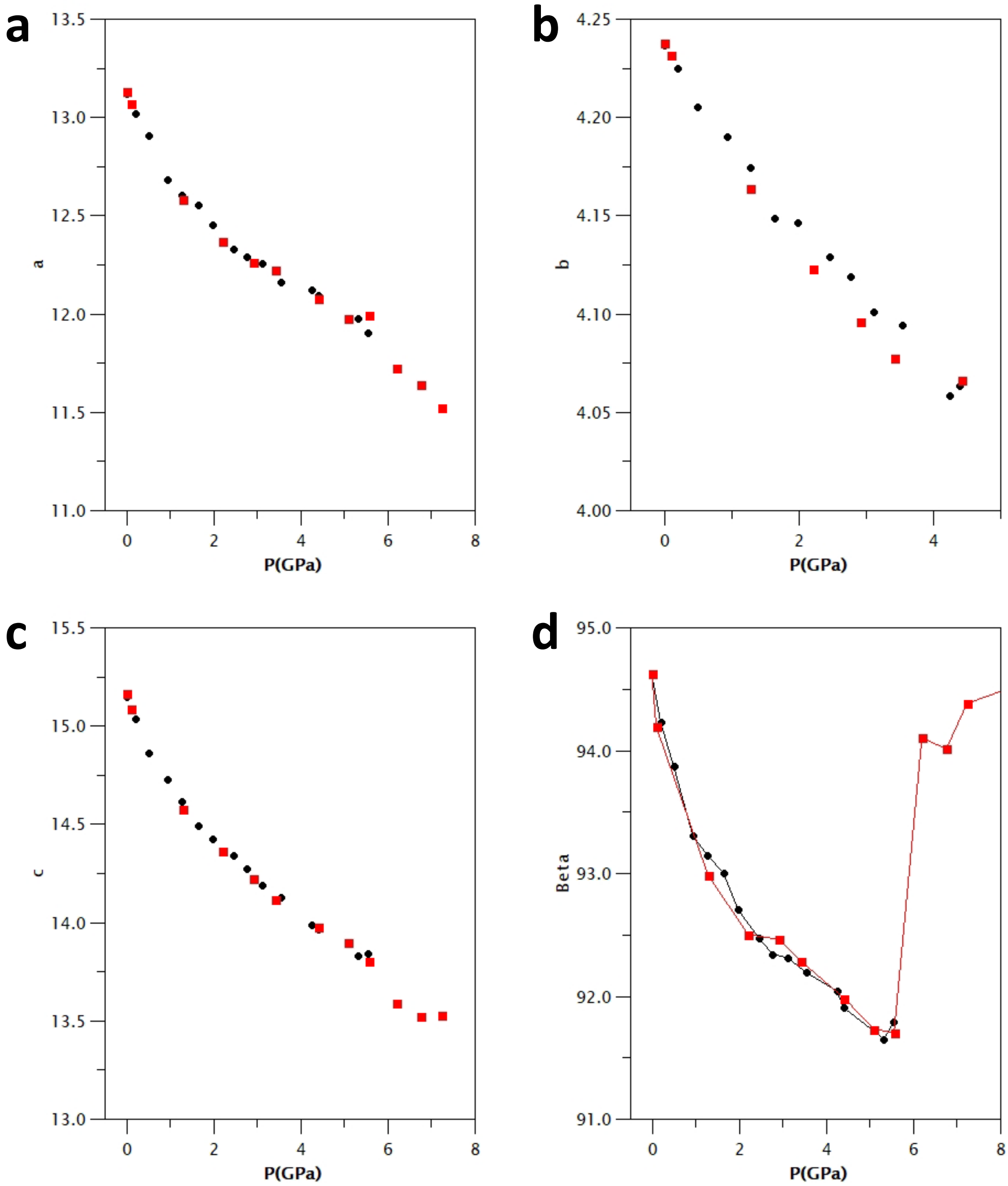

Figure S5. Evolution of cell parameters *a* (a), *b* (b), *c* (c) and *beta* (d) with pressure for compound **1** (black) and **1’** (red). Cell axis distances are expressed in Å; the *β* angle, in degrees.

Figures S5 and S6 present the behavior of the cell parameters with pressure. The *b*-axis is substantially stiffer than *a* and *c*-axes. At around 6 GPa we can observe a discontinuity on the evolution of volume with pressure and a leap on the *β* angle. It is associated with a reversible isosymmetric phase transition, stating as a first order transition where there is no change in the space group.

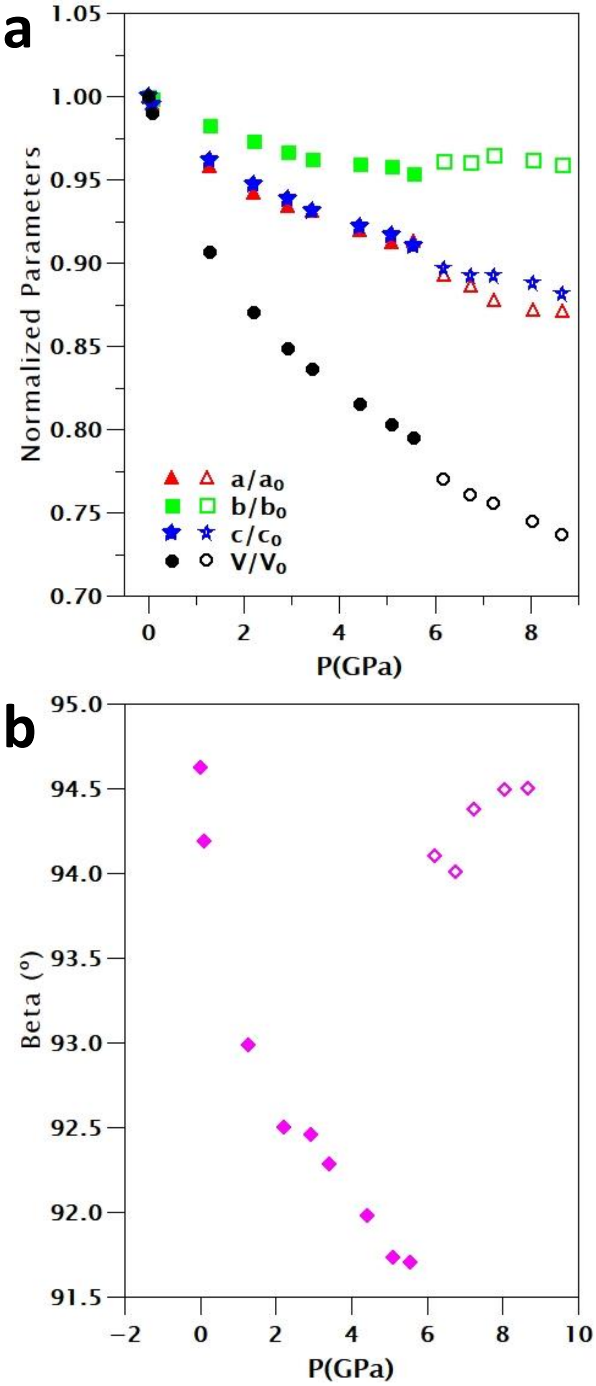

Figure S6. Variation of the cell parameters of **1’** with pressure. Error bars are smaller than their respective size symbols. Empty symbols represent the parameter after phase transition.

For equations of state (EoS) calculations we have selected the 3rd-order Birch-Murnaghan (BM) EoS according with the information obtained from the plots of *V* unit-cell parameters as normalized pressure (*F*) pressure against finite strain (*f*) (i.e. *f*-*F* plots). The *f*-*F* plots for unit-cell parameters exhibits a curvature at low pressures indicating that values at zero pressure are not strictly consistent with the higher-pressure data. However, comparison of data collected from crystals within the DAC but without pressure fluid and data from crystals in air, shows that the formal uncertainties obtained for the unit-cell parameters are underestimated, and this accounts for the observed curvature in the *f*-*F* plots.

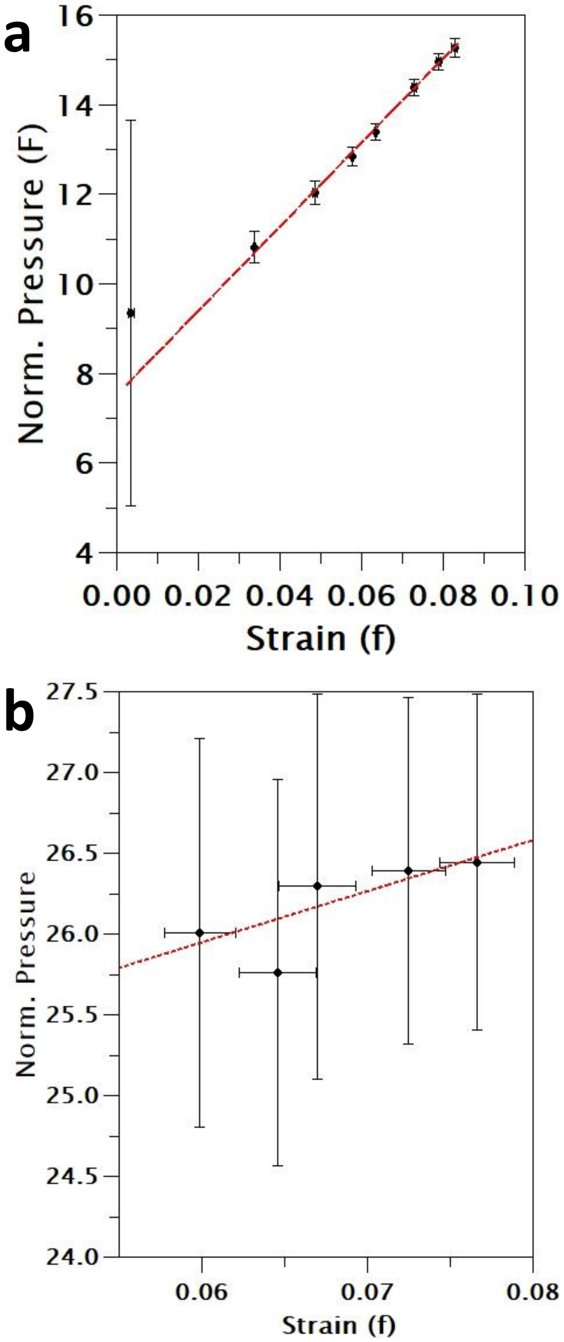

Figure S7. *f*-*F* plots for Volume for **1’** before (a) and after phase transition (b).

The fitting procedure was done with the ***EosFit7-GUI*** program[S1-S5] using the BM EoS. The refinements of EoS all yield $w\chi^2 < 1$ because of the over-estimation of the $\sigma(P)$, but none of the fits show any systematic variation of P_{obs}-P_{calc} with pressure, indicating that the reported parameters represent the data well. Lines on Figure S7 show the fitted EoS models.

The bulk modulus obtained for $C_5H_3CuINCl_2$ before 6GPa is softer than other similar copper iodide Cu-I ladders that have recently been studied under hydrostatic pressure, reporting values of 10.2(2) and 14.1(3) GPa for K_0 while 8.1(3) and 7.4(2) for K'_0 (Aguirrechu *et al.*,[S6] Conesa-Egea *et al.*[S7]). In general, these lower values are attributable to deformability of the intermolecular interactions present in the structure. The situation changes dramatically after 6 GPa where the bulk modulus increases by a factor of 3 (Figure S8).

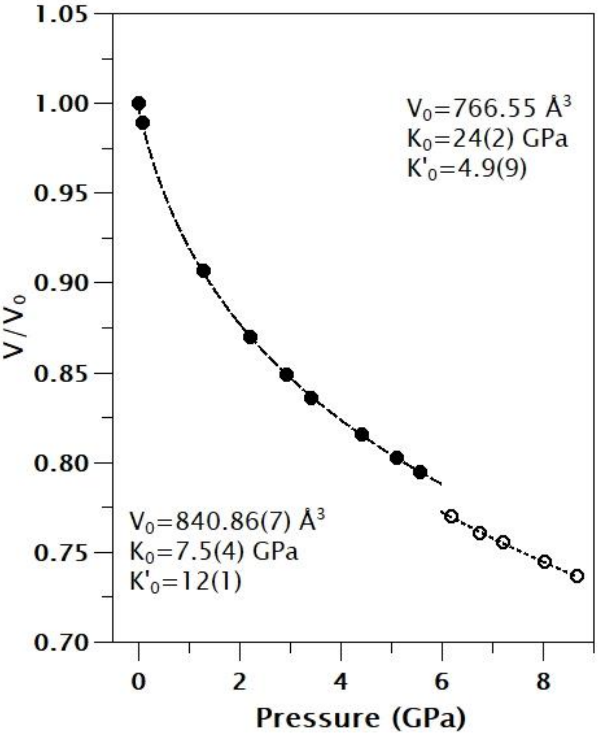

Figure S8. *EoS* fitting for **1'** before and after phase transition.

Figures S9 and S10 present the behavior of the main bond distances and angles with pressure. The evolution of these parameters shows that the main changes produce a slight deformation of the Cu-I ladders. It is clear the different behavior after phase transition of the compound where the pyridine ring suffers a tilting and rotation.

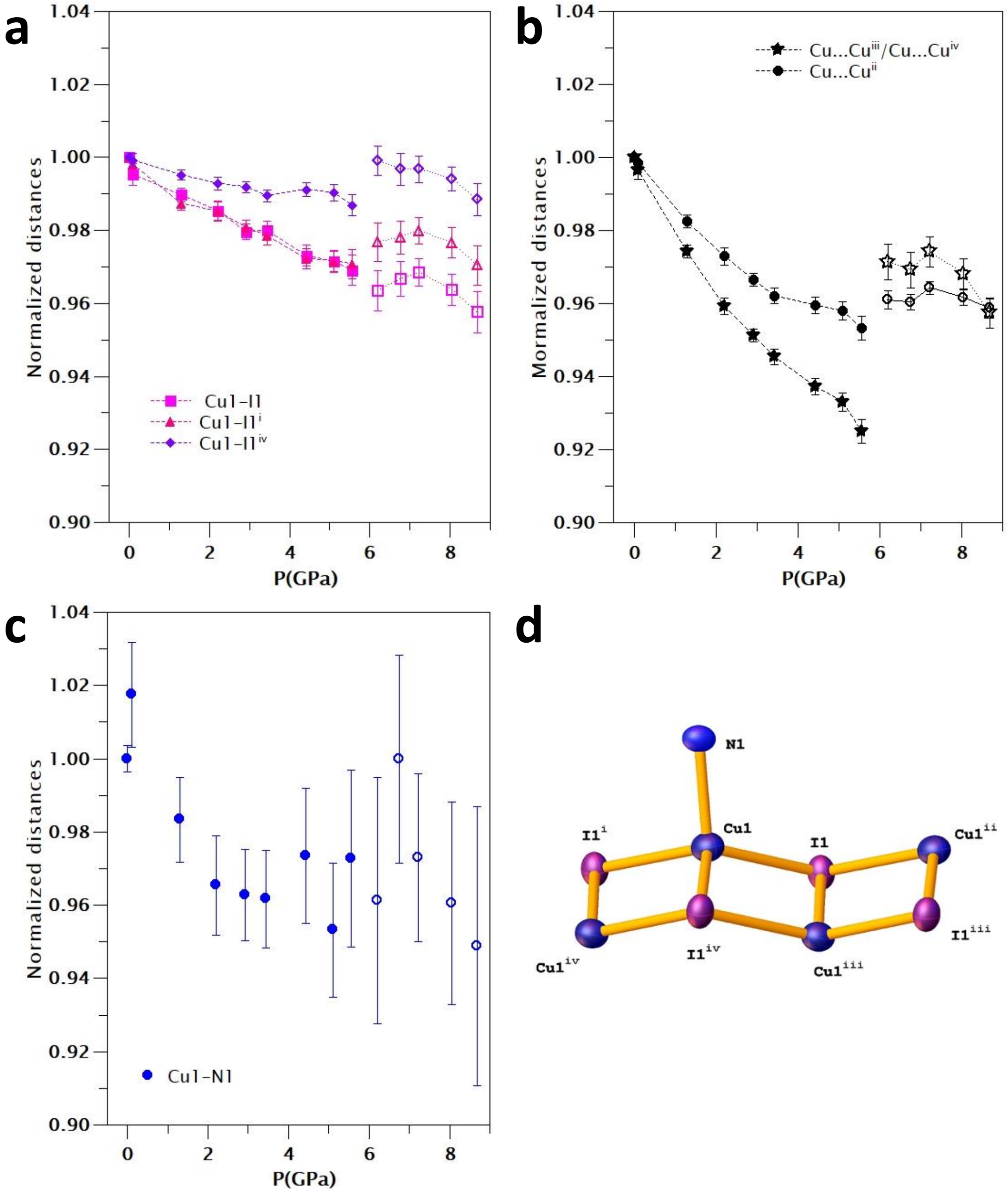

Figure S9. (a-c) Variation of the main distances on the Cu-I staircase. Error bars represent the standard for each value. (d) Referential fragment of the Cu-I staircase motif.

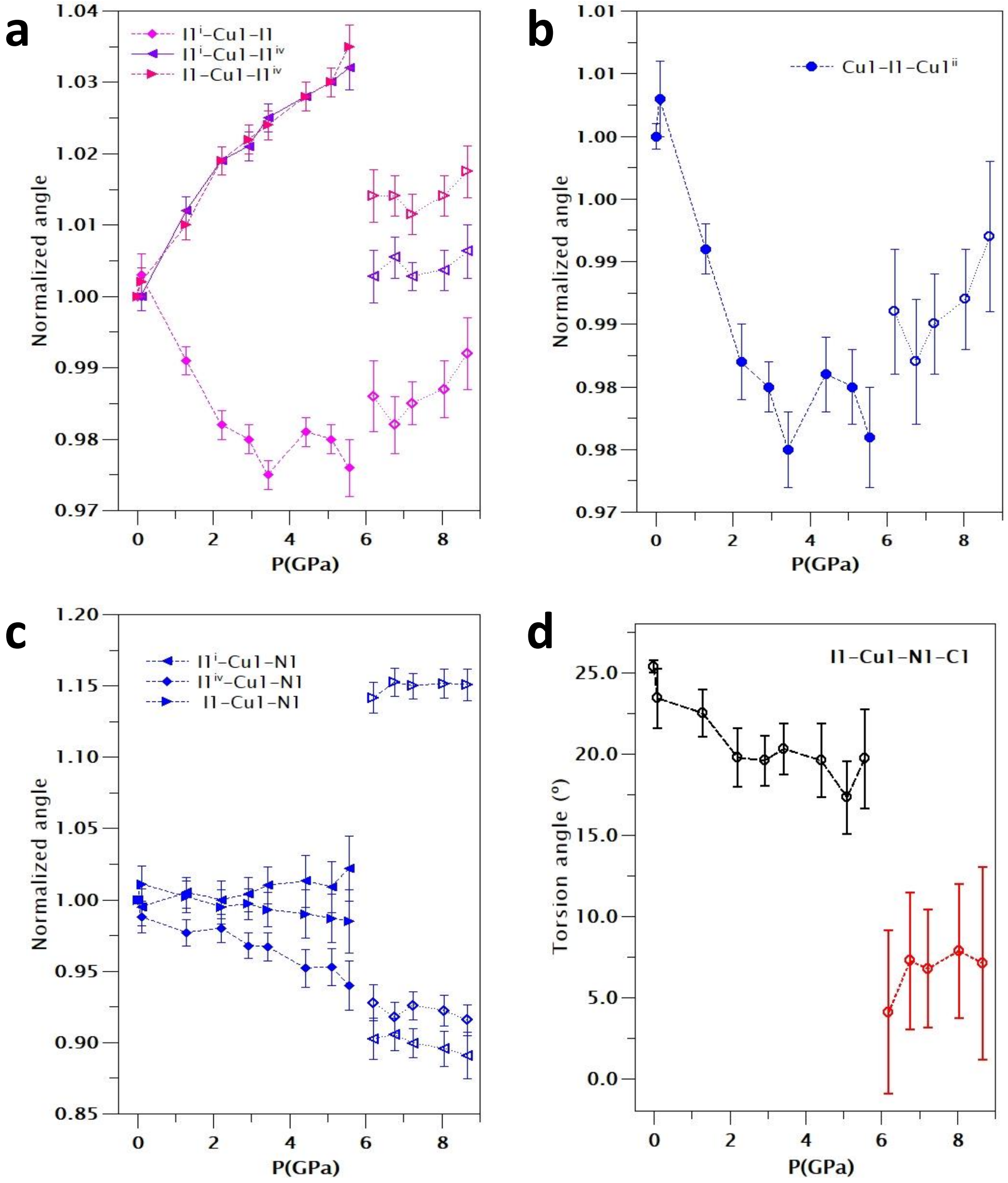

Figure S10. Variation of the main angles on the Cu-I ladder. Error bars represent the standard for each value.

The structure presents a weak π-π stacked interactions between pyridine rings with Cg…Cg from 4.238(3) to 4.041(16) Å. Also, there is a C4-Cl2…Cg from 3.640(2) Å to 3.210(18) Å that change to 2.84(3) Å. After phase transition appears a C1-H1…Cg weak interaction with C…Cg around 3.25(3) Å (Figure S11).[S8]

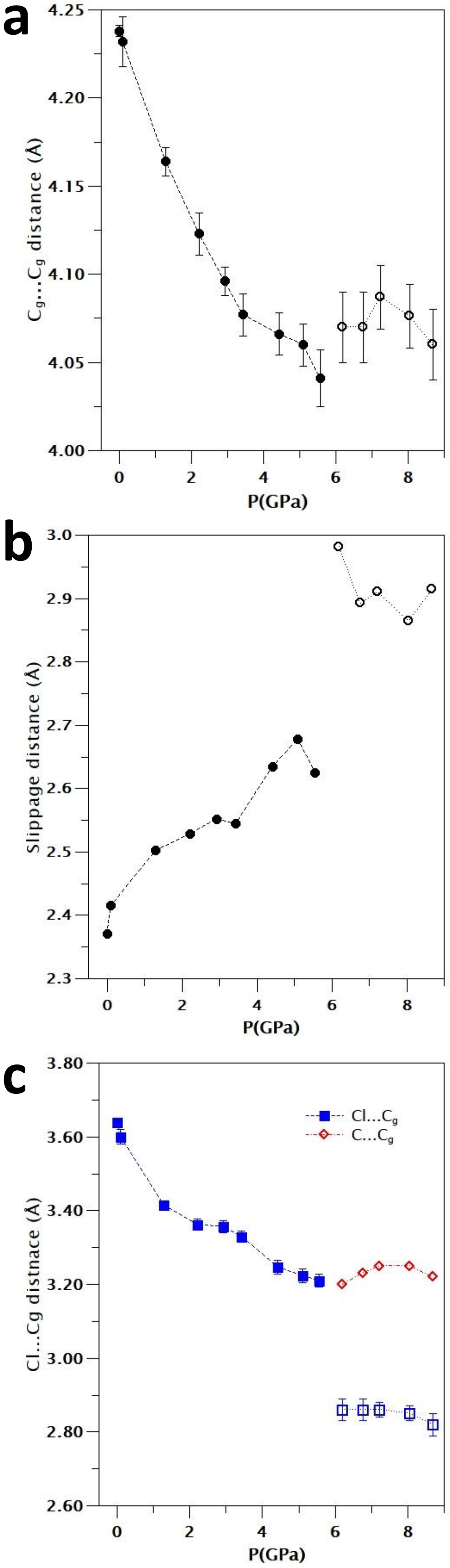

Figure S11. Variation of the Cg…Cg distances with pressure.

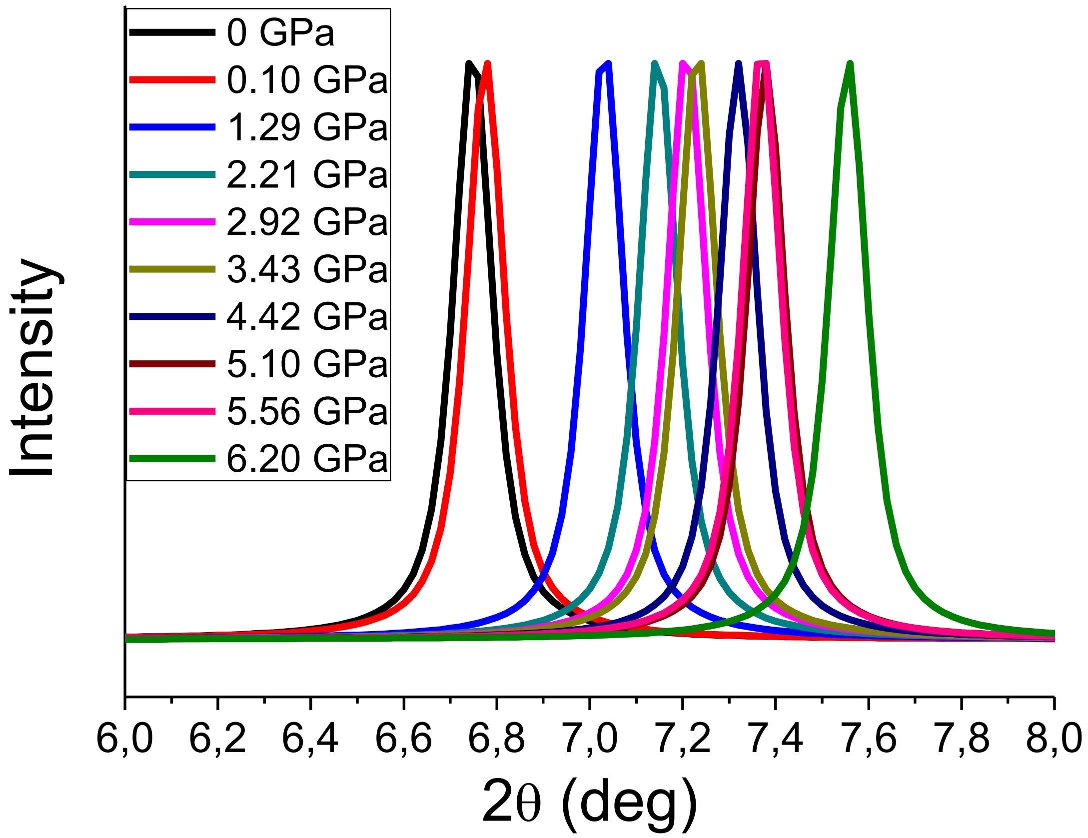

Figure S12. Theoretical PXRD of **1** at different pressures, showing the diffraction peak corresponding to the (100) planes.

Table S3. Variation of Cu···Cu distances and I-Cu-I and Cu-I-Cu angles for compound **1'** with pressure.

Distances (Å) and angles (°)	**1'** (0 GPa)	**1'** (5.56 GPa) (variation w.r.t. 0 GPa)	**1'** (6.20 GPa) (variation w.r.t. 0 GPa)
Cu-Cu^{ii}	2.8118(8)	2.602(9) (-7.5%)	2.73(1) (-2.8%)
Cu-Cu^{iii}	2.8118(8)	2.602(9) (-7.5%)	2.73(1) (-2.8%)
I1-Cu1-I1^{i}	106.16(2)	103.6(5) (-2.4%)	104.7(7) (-1.4%)
I1-Cu1-I1^{ii}	116.95(2)	121.0(3) (+3.4%)	118.6(4) (+1.4%)
I1^{i}-Cu1-I1^{i}	114.68(2)	118.4(3) (+3.2%)	115.0(4) (+0.3%)
Cu1-I1-Cu1^{ii}	64.63(2)	60.7(2) (-6.0%)	63.8(3) (-1.2%)
Cu1^{ii}-I1-Cu1^{ii}	63.73(2)	59.9(2) (-6.0%)	62.5(3) (-1.9%)

Symmetry codes: i) x-1, y, z; ii) -x, -y, -z+1; iii) -x+1, -y, -z+1

S2. Thermal behavior of 1 and 1’.

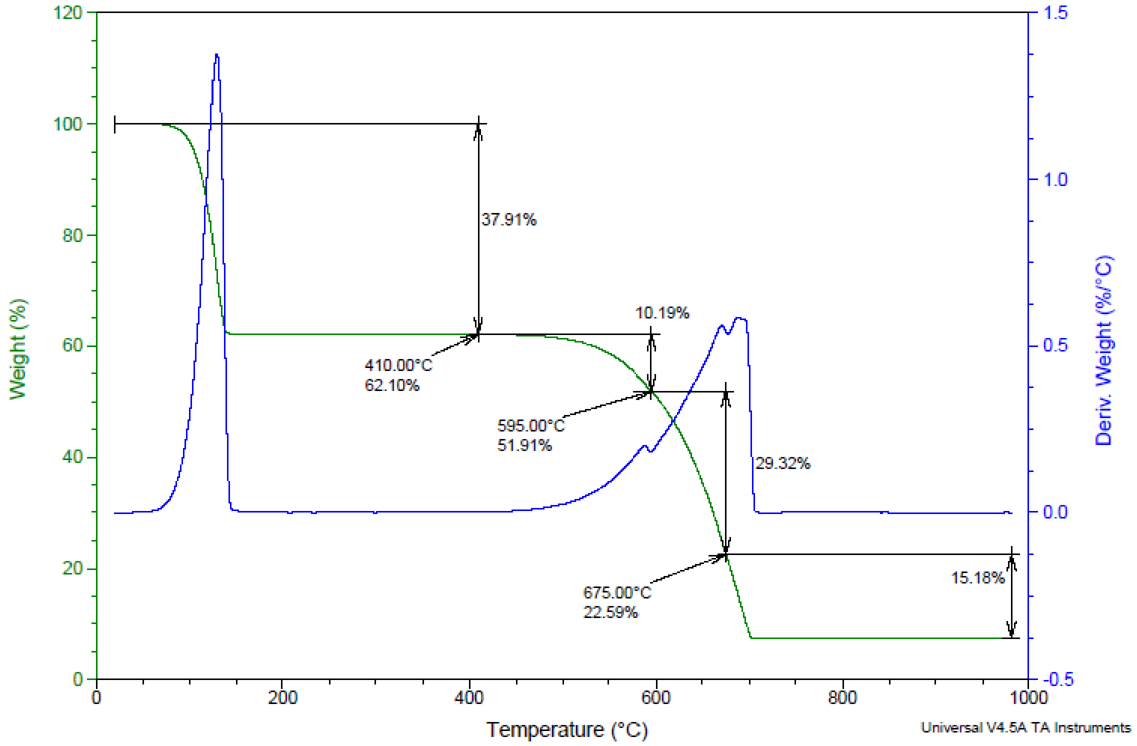

Figure S13. Thermogravimetric analysis of compound **1** at a heating rate of 10 K·min^{-1} under a nitrogen flow rate of 90 mL·min^{-1}.

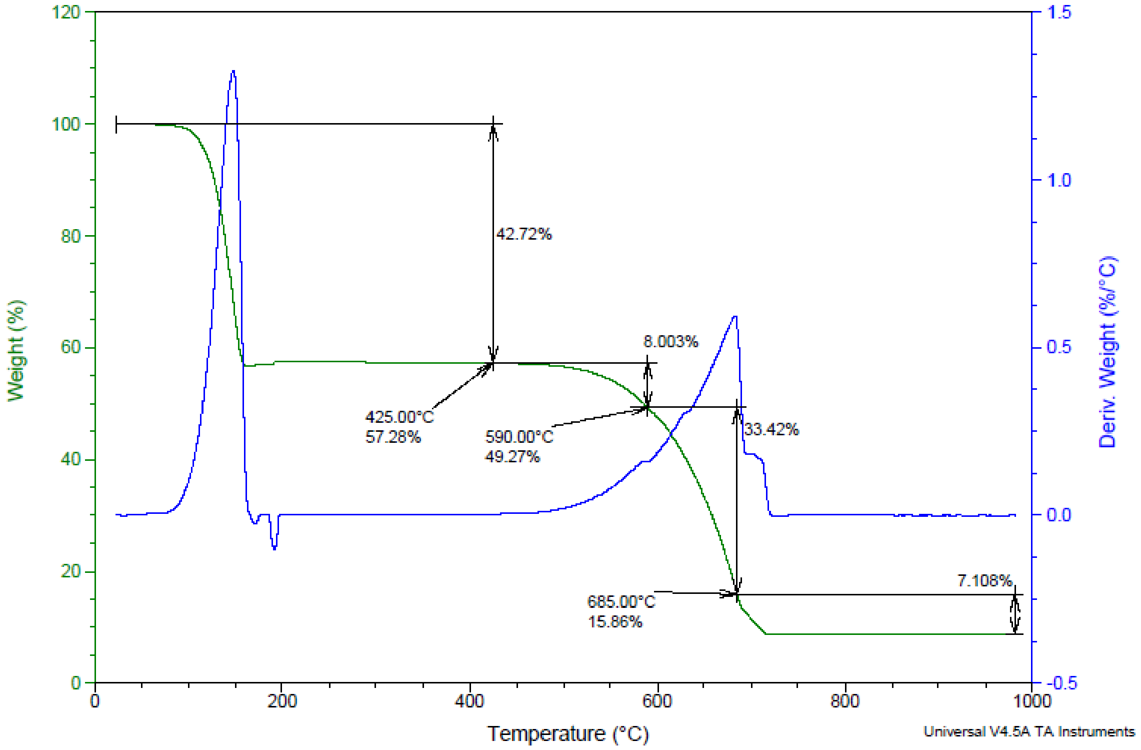

Figure S14. Thermogravimetric analysis of compound **1’** at a heating rate of 10 K·min^{-1} under a nitrogen flow rate of 90 mL·min^{-1}.

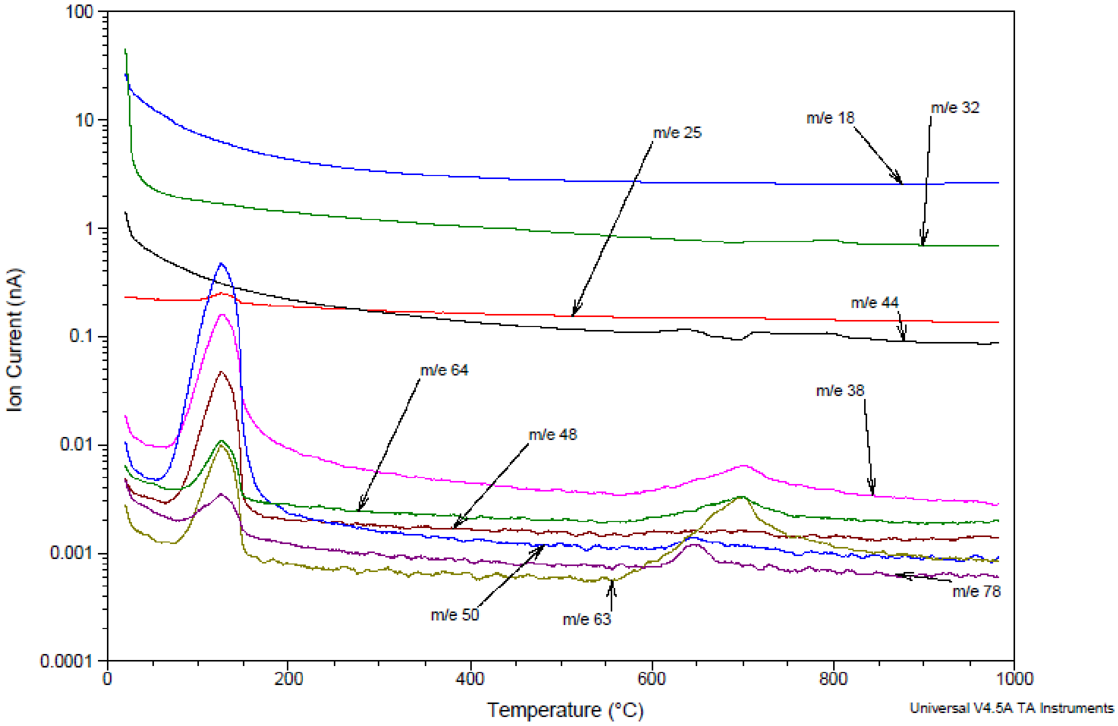

Figure S15. TG-MS analysis of compound **1** at a heating rate of 10 K·min^{-1} under a nitrogen flow rate of 90 mL·min^{-1}. The ions detected between 80 and 150 °C correspond to different fragments of the 3,5-dichloropyridine ligand.

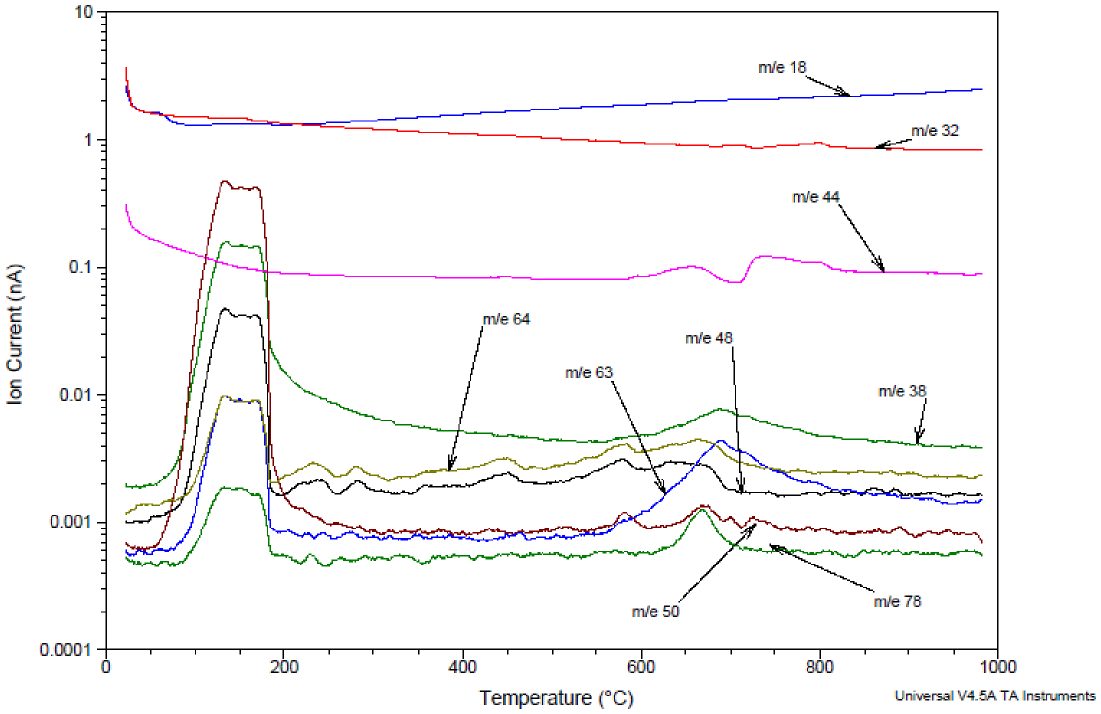

Figure S16. TG-MS analysis of crystlas of **1’** at a heating rate of 10 K·min^{-1} under a nitrogen flow rate of 90 mL·min^{-1}. The ions detected between 80 and 150 °C correspond to different fragments of the 3,5-dichloropyridine ligand.

Both forms of **[Cu(Cl$_2$-py)I]$_n$** decompose following the same mechanism. The first loss, occurring between 80 and 150-200 °C, corresponds to 3,5-dichloropyridine, which rapidly decomposes into different fragments in the ionization system (theoretical loss: 43.7 %; the loss registered for **1'** is accurate with the theory, but the one for **1** is lower than expected, probably due to some rests of copper(I) iodide in the sample). Afterwards, between 400 and 750 °C, a second loss is registered, due to some copper (detected as Cu$^+$), iodine (detected as I^{2+}) and volatile Cu-I compounds.

S3. Infrared spectroscopy of 1 and 1'.

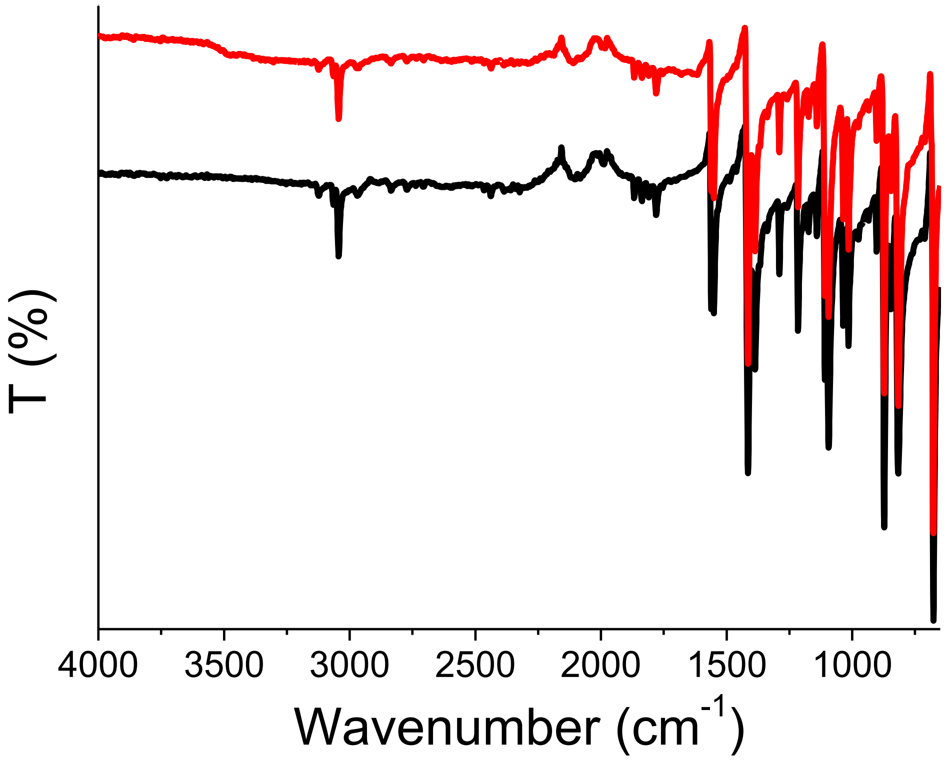

Figure S17. ATR FT-IR spectra of **1** (black) and **1'** (red).

S4. XPS studies of 1 and 1'

Table S4. Binding energy (BE) values of **1** and **1'**.

Compound \ BE (eV)	**C 1s**	**Cl 2p**	**Cu 2p$_{3/2}$**	**I 3d**	**N 1s**	**Cu Auger parameter***
1	284.8	200.3	932.3	619.3	398.0	1848.7
1'	284.8	200.2	932.3	619.3	397.9	1848.6

*Auger parameter = 1253.6 + BE Cu2p$_{3/2}$ – BE Cu Auger[S9]

S5. ^{1}H- NMR measurements.

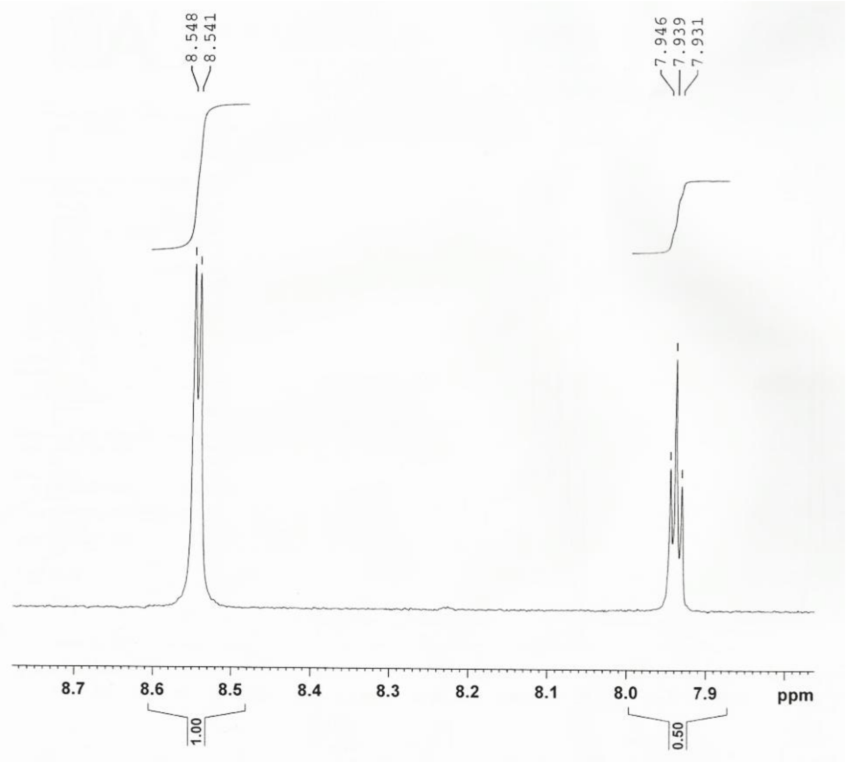

Figure S18. ^{1}H-NMR spectrum of commercial Cl_2-py in CD_3CN.

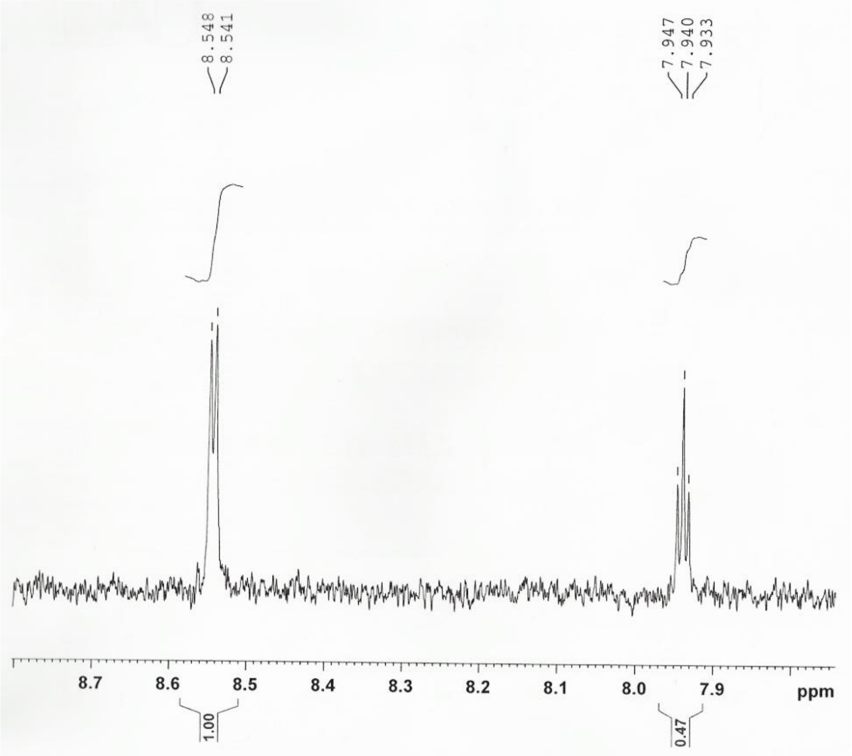

Figure S19. ^{1}H-NMR spectrum of Cl_2-py treated in solvothermal conditions (acetonitrile, 120 °C, 72 hours) in CD_3CN. The high noise levels are due to a low sample concentration.

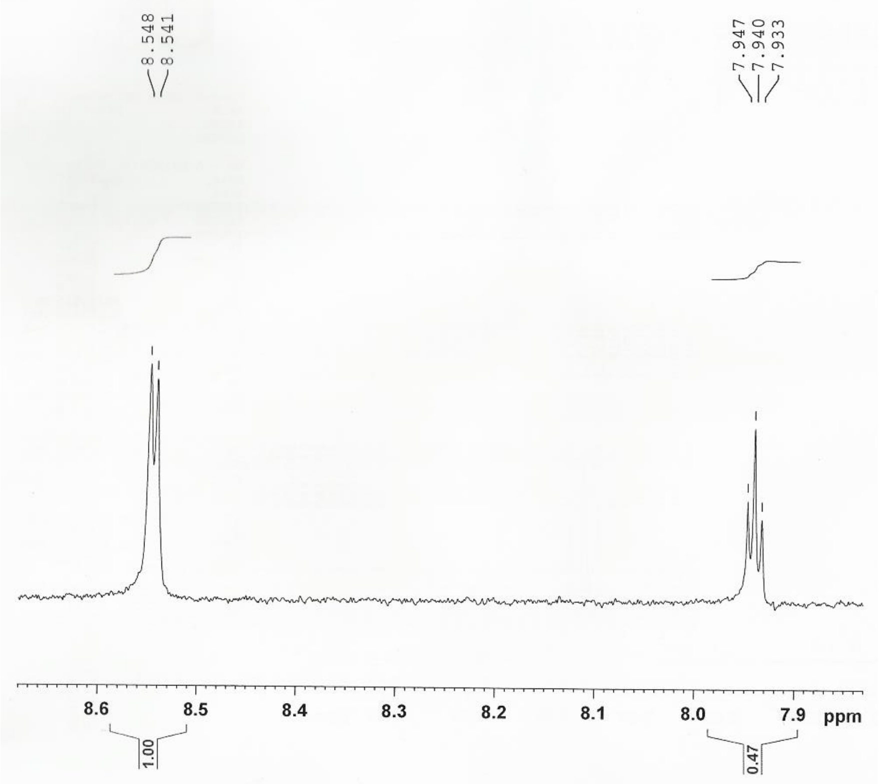

Figure S20. ^{1}H-NMR spectrum of redissolved crystals of **1** in CD_3CN.

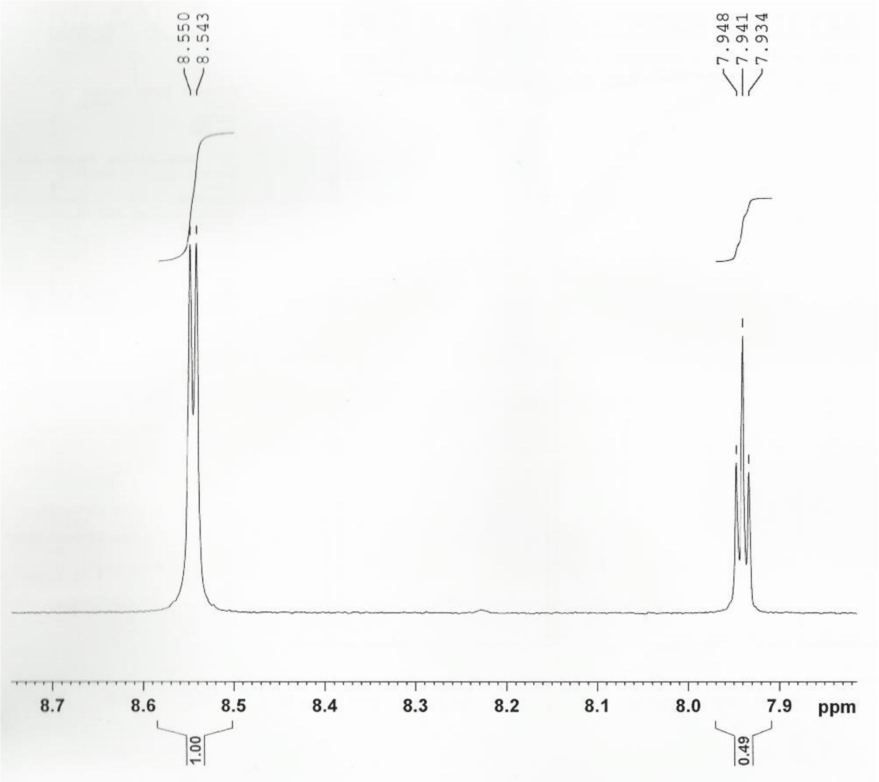

Figure S21. ^{1}H-NMR spectrum of redissolved crystals of **1’** in CD_3CN.

S6. Characterization of the reaction medium leading to the formation of 1’

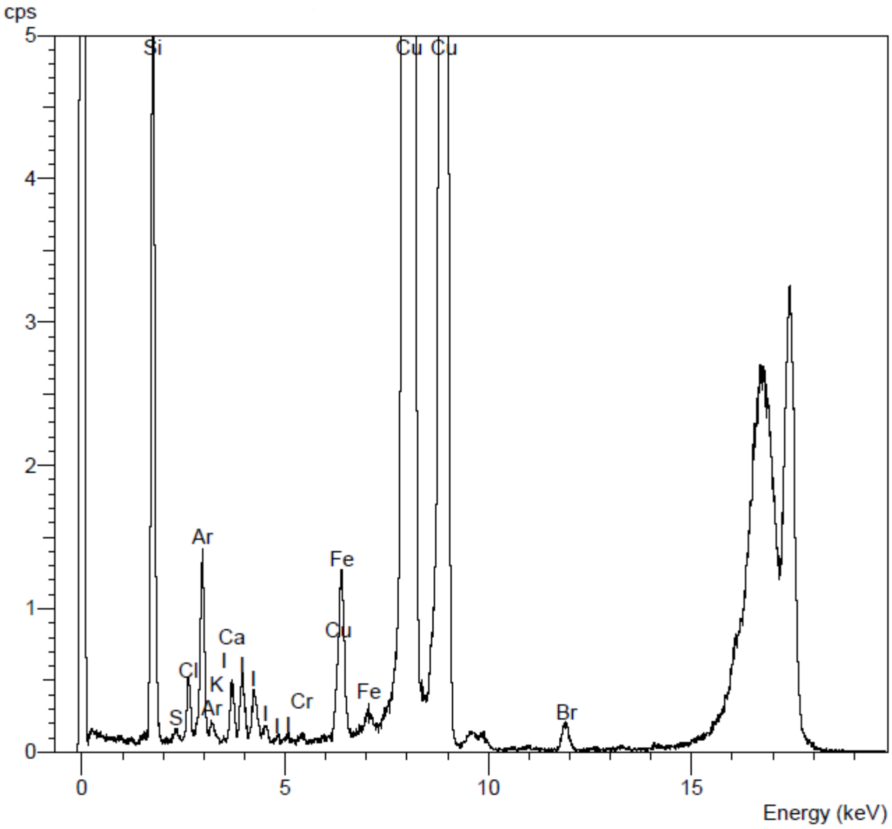

Figure S22. TXRF spectrum of the residual brown solid obtained in the synthesis of **1’**.

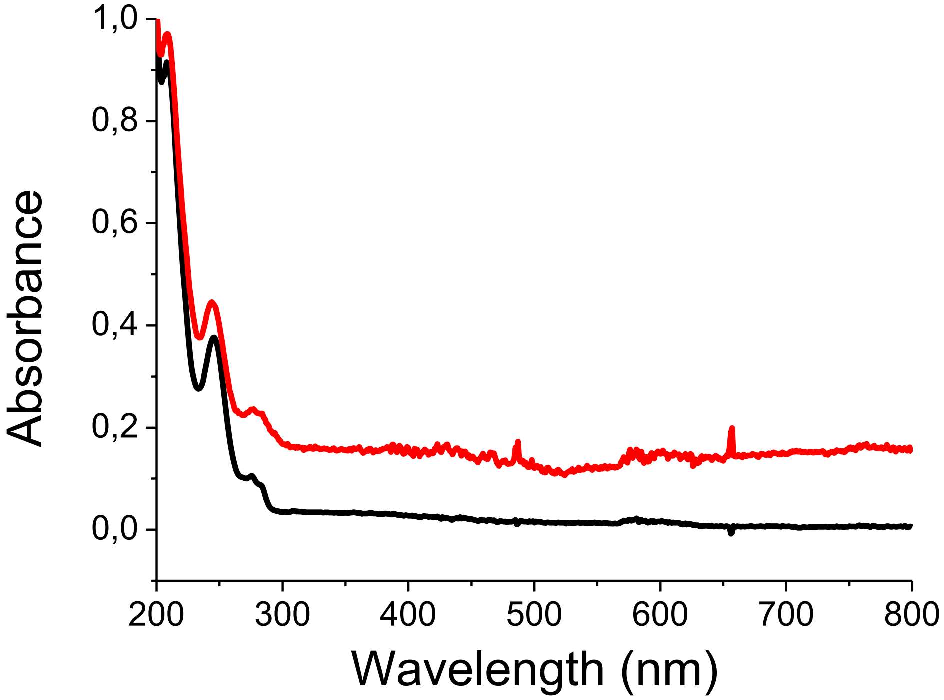

Figure S23. UV-visible spectra of the reaction solutions of **1** (black) and **1’** (red).

S6.1. Extra elemental analyses of 1 and 1’

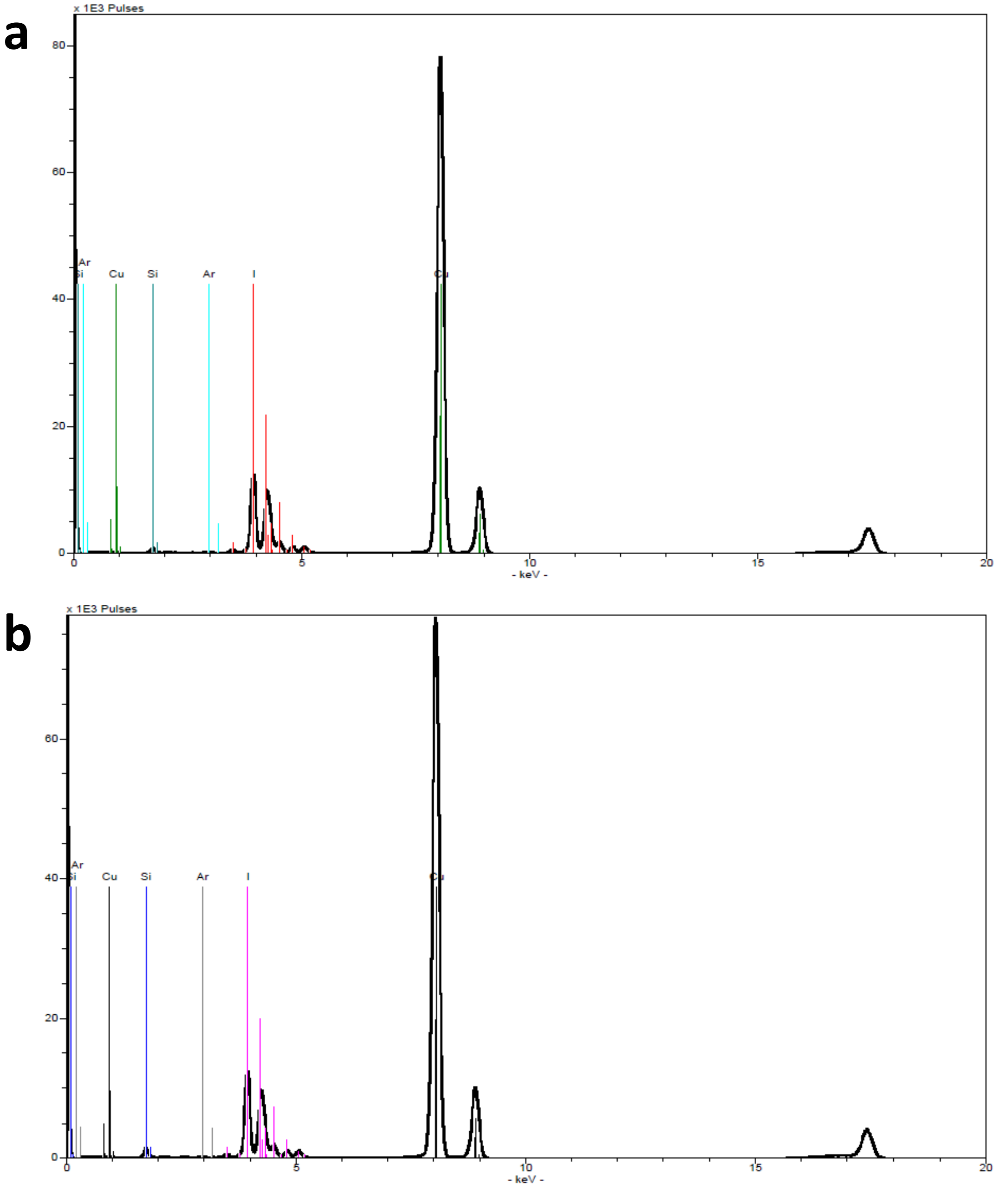

Figure S24. TXRF analysis of **1** (a) and **1’** (b).

Table S5. Mass-proportion TXRF analysis of compounds **1** and **1’**.

Element	Concentration (rmu), **1**	Concentration (rmu), **1’**
Cu	100.000	100.000
Cl	0.34 ± 0.09	0.40 ± 0.09
Fe	0.051 ± 0.007	0.040 ± 0.007
Ni	0.034 ± 0.006	0.011 ± 0.006
Br	0.017 ± 0.001	0.015 ± 0.001
I	187.2 ± 0.3	185.3 ± 0.3

rmu = Relative Mass Unit

Table S6. Semi-quantitative analysis by Inductively Coupled Plasma-Mass Spectrometry (ICP-MS) of compounds **1** and **1’**.

Element	Concentration (µg/g)	Intensity	Concentration (µg/g)	Intensity
CP	1	1	1’	1’
Na	**98.53**	**11672.00**	**11.63**	**1292.00**
Mg	**4.35**	241.00	**0.00**	**0.00**
Al	**5.84**	94.00	**7.82**	**118.00**
Si	**45.54**	929.00	**28.22**	**540.00**
K	**13.8**	629.00	**7.95**	340.00
Ca	**51.92**	4362.00	**27.87**	2196.00
Fe	**10.28**	4480.00	**0.52**	212.00
Cu	**174190.51**	176916299.00	**163250.11**	155441910.00
Zn	**38.20**	10445.00	**24.63**	6312.00

Table S7. Atomic absorption measurements of copper in samples of **1** and **1’**.

Coordination Polymer	Cu(%)	Standard error
1	18.81	0.97
1’	18.85	0.20

S7. Morphological studies of 1 and 1’.

A morphological study using SEM allows observing the initial form and dimensions of crystals **1** and **1’** obtained through the use of different synthetic conditions. Both **1** and **1’** form crystals with the shape of big blocks with lengths of (1.0 ± 0.5) mm for **1** and (5 ± 2) mm for **1’**.

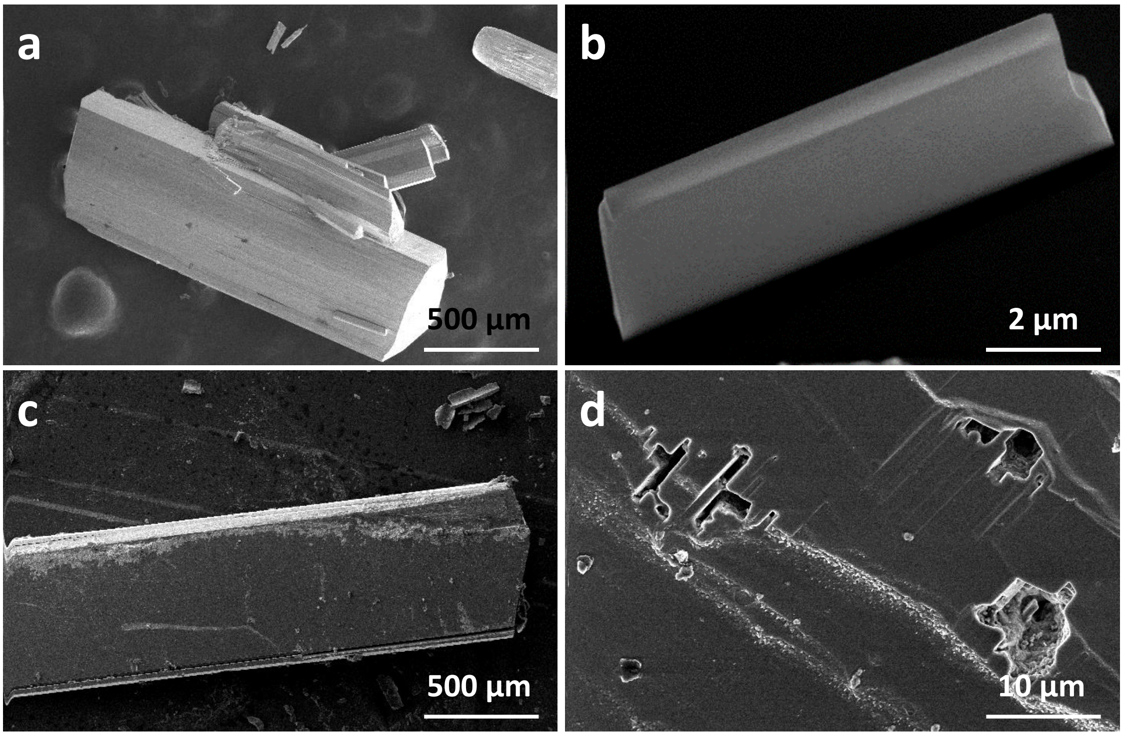

Figure S25. SEM images of **1** crystals obtained by slow evaporation of the mother liquor (a) or directly from the reaction medium (b). General (c) and detailed (d) SEM images of a **1’** crystal.

S8. Luminescent behavior of 3,5-dichloropyridine.

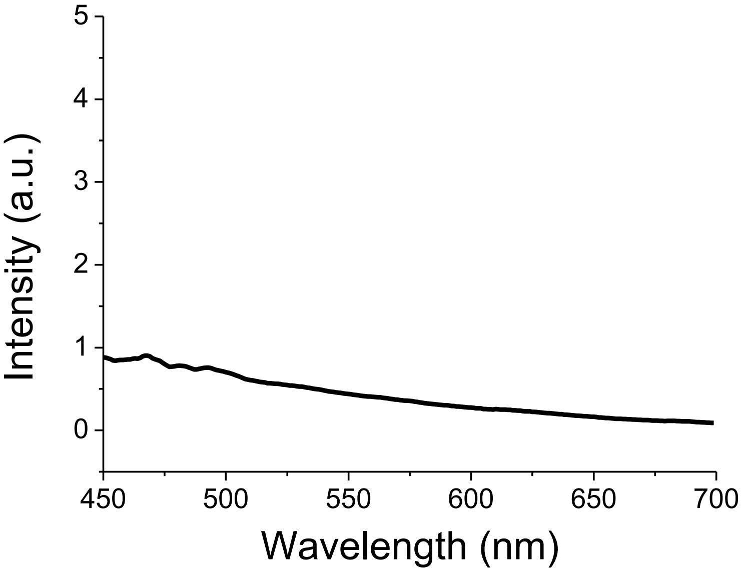

Figure S26. Luminescence spectrum of 3,5-dichloropyridine.

S8.1. Mechanochromism studies of 1 and 1’.

Finally, we have also evaluated the emission properties of **1** and **1’** under hydrostatic pressure on **1** and **1’** crystals inside a diamond anvil cell (Figure 7). **1** shows an interesting behavior, in which the direct band gap emission band is quenched at low applied pressures of 1 GPa. In contrast, **1’** shows negligible changes in the low-energy band, while the direct band gap emission also disappears at pressures >5.3 GPa. Interestingly, the low-emission band becomes brighter at applied pressures >6 GPa.

In order to understand the deactivation of the direct band gap emission under pressure, we first analyze the powder X-ray diffraction patterns of the pressed pellets of **1** after applying 5 GPa for 2 min. They show neither amorphization nor displacements of the signals with respect to the pristine crystals (Figure S4). These results indicate that the changes suffered by **1** are reversible and only appreciable immediately after pressures are applied. Indeed, the emission is recovered after relishing the applied pressure. Next, we carried out the same analysis under different pressures (Section S1.3, Figures S5-S11). This allowed us to calculate the equations of state (EoS) and bulk modulus of **1** and **1’**, indicating the degree of compressibility of these materials. Since **1** deteriorated at low pressures, and considering the alike behavior and crystal structures of **1** and **1’**, the latter was taken as the reference for these studies. Its bulk modulus (K_0 = 7.5 ± 0.4 GPa) is substantially smaller than the lower limit of the range expected for organometallic compounds (10-20 GPa), as a consequence of the deformability of the intermolecular interactions present in the structure. At pressures above 6 GPa a first order phase transition occurs, implying an isosymmetric transition without change of the space group. In these conditions, the bulk modulus triples its value, reaching K_0 = 24 ± 2 GPa. Therefore, after the phase transition the single crystal of **1’** loses elasticity, with reversible effects as pressure is released.

The increase of pressure induces a significant variation in some distances and angles of the structure (Table S3, Figure S9). On one hand, the evolution of these parameters shows that the main changes produce a slight deformation of the Cu-I ladders. The softest distances are those of Cu···Cu interactions, being reduced significantly (up to a 7.5 % at 5.56 GPa) close to the point where the phase transition occurs. On the other hand, Cu-I bonds are stiffer (Figure S9). Cu-I-Cu and I-Cu-I angles along the chains also suffer important distortions, these ones lying between 3 and 4°. As usual for this kind of compounds, the layers maintain their planarity and orientation but the small displacement of the ligands over one another appears to be the cause for the changes in angles and, therefore, in the unit-cell parameters. As above mentioned, the behavior of these compounds is reversible, returning to the initial distances and angles at 0 GPa. The theoretical X-ray powder diffraction patterns obtained at different pressures allow the visualization of the variation in the diffraction peaks as a consequence of the modifications in the lattice parameters, distances and angles (Figure S12).

At pressures >6 GPa the crystals suffered a phase transition highlighted by i) the shortenings of distances and the modifications in the angles that are partially reverted, ii) the asymmetry of the Cu-I changes, and iii) the stiffness of the structure. When pressures are far above this point, distances and angles along the chains suffer changes almost negligible compared to those suffered at lower pressures.

Thus, the pressure dependent photoluminescence highlighted by the deactivation of the direct band emission is attributed to the above described decrease in structural network parameters involving i) a reduction of the volume of the cell in almost 20% and ii) a shortening in the Cu-I and Cu-Cu distances that produce a distortion in the angles, increasing the interligand interactions.[S7,S10] In line with the increase in the intensity of the low-energy emission band in **1’** at pressures >6 GPa, the most likely rationale is the change of the phase transition that enhances the radiative rate constant from defected states. Finally, the reversible emission behavior is in perfect agreement with the high flexibility of this type of Cu-I chains, where the small structural changes that occur when exerting pressure are usually reverted when it is stopped.[S7,S11] However, it is very striking that the structural defects are not affected by both thermal and pressure stress scenarios.

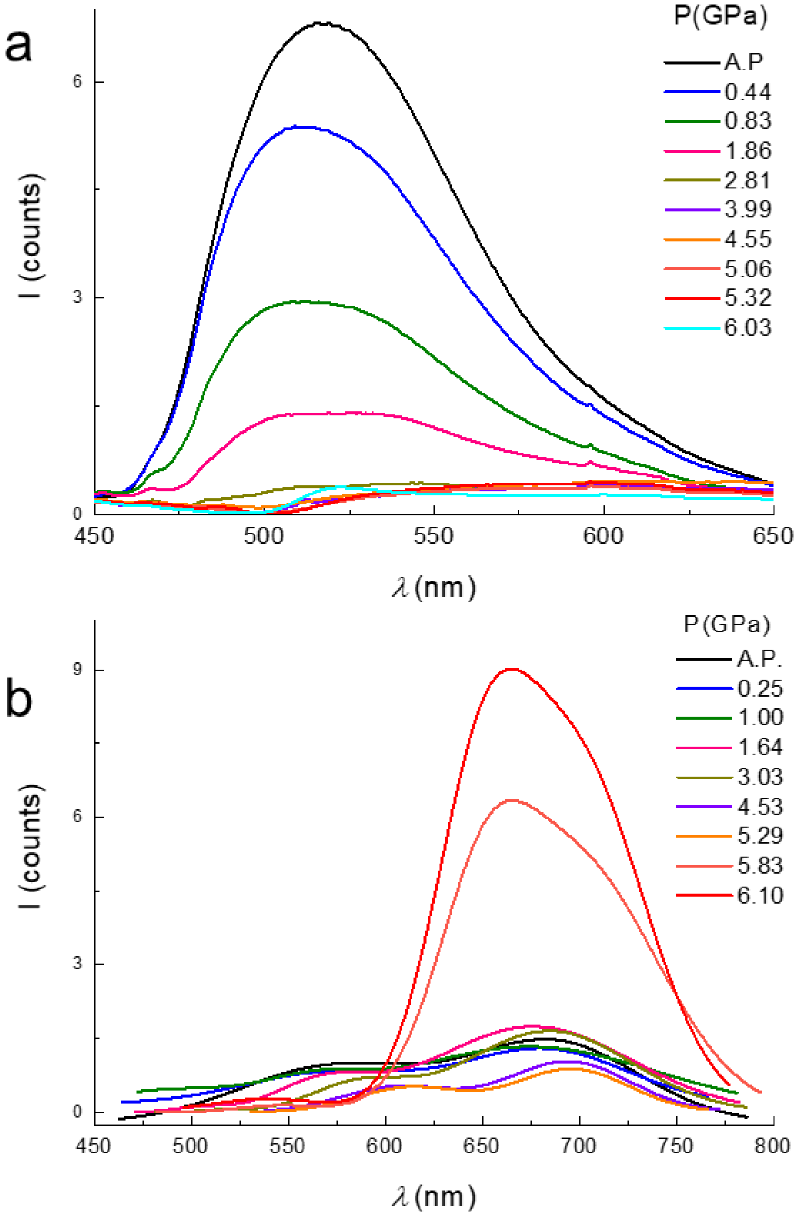

Figure S27. Pressure dependence of the emission spectra (λ_{exc} = 375 nm) of **1** (a) and **1’** (b).

S9. Theoretical calculations.

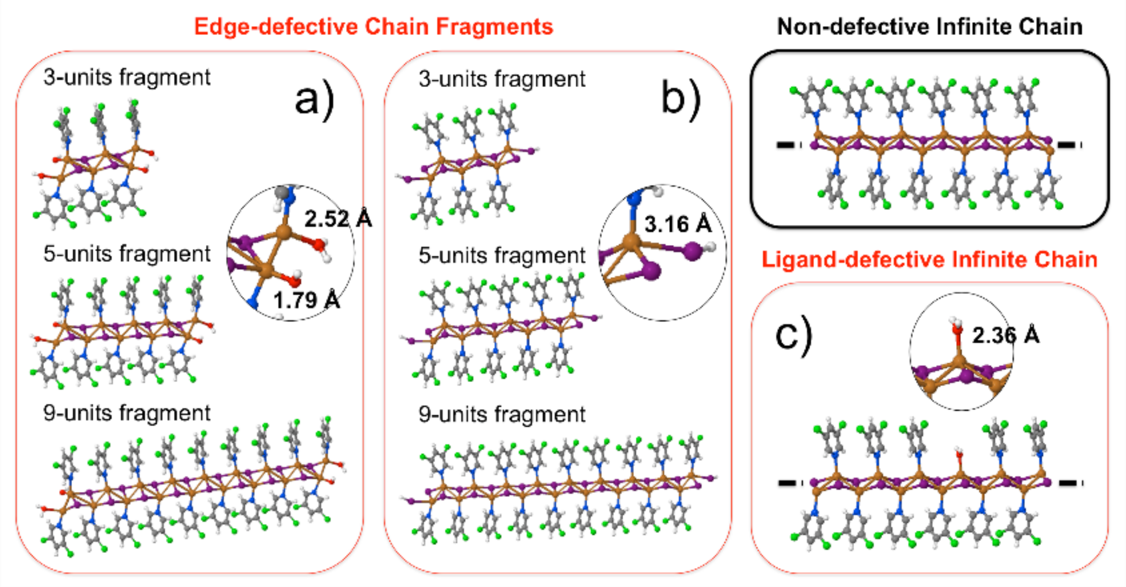

Figure S28. Pictorial views of the pristine infinite chain of the compound as obtained by the X-ray diffraction experiment (right-top panel). a) and b) Computed optimized structures for two 3, 5, and 9-units defective chain fragments with two different terminating effects. c) Computed optimized structure for an infinite defective chain with a lack of organic ligands (with a density of defects of 1/12). Most representative distances are shown superimposed.

S10. Electrical conductivity and sensing behavior to acetic acid vapors.

Conductivity measurements were carried out in order to study the sensibility change in the conductivity of **1** and **1’** upon the exposition to acetic acid vapors. Interaction was demonstrated by the change in the conductivity of **1** and **1’** by Electrochemical Impedance Spectroscopy (EIS).

The conductivity values σ (Scm^{-1}) were determined from the Nyquist plot by arc extrapolation to the Z’ real axis on the low frequency side. Each plot shows the presence of a depressed semicircular arc at high-medium frequencies (1 MHz-1 Hz), which is attributed to the bulk properties of the compound. The shapes of the Nyquist plots recorded after different exposure times for both **1** and **1’** compounds are similar; however, the intercept of the semicircle with the Z’ axis shifts towards lower Z’ values with increasing exposition time (Figure S28).

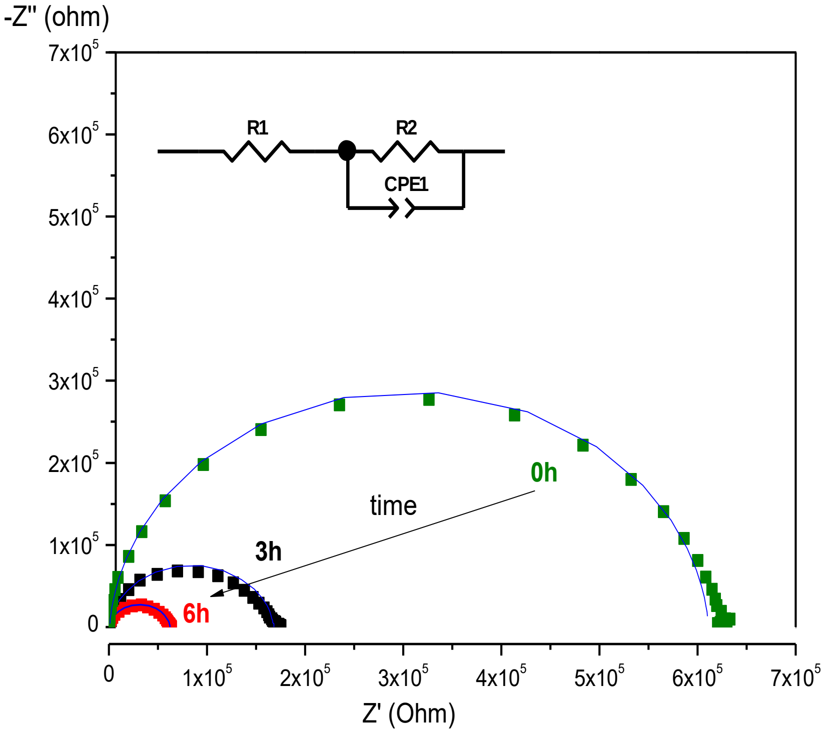

Figure S29. Nyquist plot of **1** after 0, 3, 6 h of exposure to acetic acid vapors at 298K, with the fitting circuit: Experimental values (■), fitting values (-).

The EIS data were fitted employing the ZView 3.1 software (Scribner Association) using equivalent circuit as shown inserted in Figure S27. The impedance measurements R_2 and CPE1 are considered the bulk resistance and the constant phase element representing a no ideal capacitance of the pellet. R_2 (Ω) is used to find the specific ionic conductivity, σ (Scm^{-1}) of the sample according to the equation:

$$\sigma = \frac{l}{A \cdot R_2}$$

where l (cm) is the thickness of the pellet and A (cm^2) represents the surface area of the sample (0.126 cm^2).

Both materials present the same behavior; σ increases (ca. 3 orders of magnitude) with increasing exposition time from values of $7 \cdot 10^{-7}$ or $1.2 \cdot 10^{-7}$ S cm^{-1} for **1** and **1’** (t= 0h) respectively to values around $1.5 \cdot 10^{-4}$ or $8 \cdot 10^{-4}$ S cm^{-1} for **1** and **1’** for (t = 24h) respectively (Figure S29) and reaches saturation after ca. 24h of exposure. Therefore, vapors of acetic acid produce a similar effect in both forms of the material.

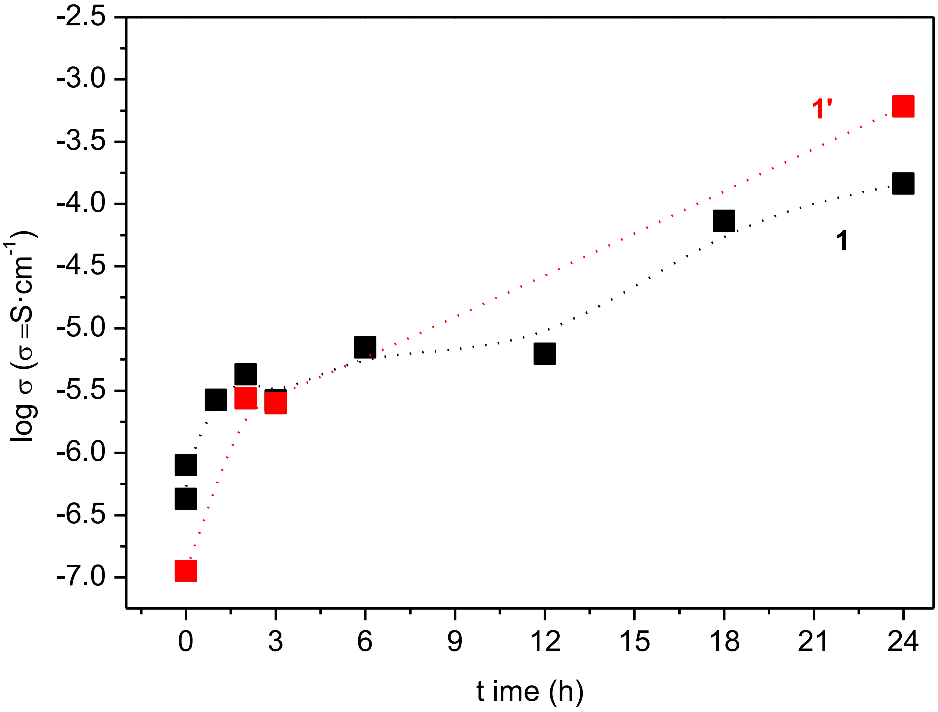

Figure S30. Electrical response of **1** (black) and **1’** (red) with different exposition time to vapors of acetic acid.

In agreement with the Bode diagram, the semicircle representing the bulk properties of compounds shifted to higher frequencies when the acetic acid exposure time increases. This fact indicates that the material/electrode interphase capacitive character becomes less important, and the highly conductive phase of **1** and **1’** appears. When saturated acetic acid pellets were exposed to air for longer times a poor value of conductivity was obtained. If we compare these results with the experiments involving different exposure times to Acetic acid vapor, the behavior clearly indicates the crucial role of the acetic acid molecules in establishing the conductivity pathway. In addition, there are not important differences between **1** and **1’**.

References

S1. J. Gonzalez-Platas, M. Alvaro, F. Nestola, R. J. Angel, *J. Appl. Cryst.*, 2016, **49**, 1377-1382.

S2. R. J. Angel, J. Gonzalez-Platas, M. Alvaro, *Z. Kristallogr.*, 2014, **229**, 405-409.

S3. E. C. Spencer, R. J. Angel, N. L. Ross, B. E. Hanson, J. A. K. Howard, *J. Am. Chem. Soc.*, 2009, **131**, 4022-4026.

S4. N. P. Funnell, A. Dawson, D. Francis, A. R. Lennie, W. G. Marshall, S. A. Moggach, J. E. Warren, S. Parsons, *CrystEngComm*, 2010, **12**, 2573-2583.

S5. C. Slebodnick, J. Zhao, R. Angel, B. E. Hanson, Y. Song, Z. Liu, R. J. Hemley, *Inorg. Chem*., 2004, **43**, 5245-5252.

S6. A. Aguirrechu-Comeron, R. Hernandez-Molina, P. Rodriguez-Hernandez, A. Muñoz, U. R. Rodriguez-Mendoza, V. Lavin, R. J. Angel and J. Gonzalez-Platas, *Inorg. Chem.*, 2016, **55**, 7476-7484.

S7. J. Conesa-Egea, J. Gallardo-Martínez, S. Delgado, J. I. Martínez, J. Gonzalez-Platas, V. Fernández-Moreira, U. R. Rodríguez-Mendoza, P. Ocón, F. Zamora and P. Amo-Ochoa, *Small*, 2017, **13**, 1700965.

S8. R. J. Angel, *Win_Strain program for Strain calculations.* (http://www.rossangel.net), **2015**.

S9. G. Moretti, F. Filippone, M. Satta, *Surf. Interface Anal.*, 2001, **31**, 249.

S10. Q. Benito, B. Baptiste, A. Polian, L. Delbes, L. Martinelli, T. Gacoin, J.-P. Boilot and S. Perruchas, *Inorg. Chem.*, 2015, **54**, 9821-9825.

S11. J. Conesa-Egea, N. Nogal, J. I. Martinez, V. Fernandez-Moreira, U. R. Rodriguez-Mendoza, J. Gonzalez-Platas, C. J. Gomez-Garcia, S. Delgado, F. Zamora and P. Amo-Ochoa, *Chem. Sci.*, 2018, **9**, 8000-8010.